ELSEVIER

The Influence of Microcracking on the Mechanical Behavior of Cement Based Materials

Eric N. Landis* and Surendra P. Shah†
*Department of Civil and Environmental Engineering, University of Maine, Orono, and †Center for Advanced Cement-Based Materials, Northwestern University, Evanston, Illinois

Quantitative acoustic emission techniques were applied to basic problems of microfracture in cement based materials. Acoustic emissions in cement based materials result from microcracks and other dynamic phenomena in the fracture process zone. The goals of this research program were to characterize microcracking in various cement based materials, to track the evolution of damage in those materials, and to examine the relationships to overall mechanical behavior. Characterizations of the microcracks showed a dependence on the degree of inhomogeneity in the material. Fine-grained materials showed different microfracture characteristics than coarse-grained materials. Microcracks were characterized according to their fracture mode. The fine-grained materials tested showed primarily mixed-mode microfracture, whereas the coarse-grained materials showed primarily mode II (shear) microfracture. It is experimentally shown that there exists a relationship between the microcrack characteristics established through quantitative acoustic emission analysis and the overall fracture toughness of the material. ADVANCED CEMENT BASED MATERIALS 1995, 2, 105–118

KEY WORDS: Acoustic emission, Fracture process zone, Fracture toughness, Microcracking

The mechanical behavior of concrete has often been attributed to a fracture process zone. This fracture process zone manifests itself in several ways: the nonlinear stress-strain behavior, the postpeak strain softening, and the increase in fracture toughness over purely brittle main (critical) crack, aggregate interlocking, crack bridging, and grain boundary sliding friction. These toughening mechanisms lead to the type of material behavior commonly associated with concrete. From a material modeling standpoint, properties of the fracture process zone must be known to accurately predict the response of the material to stress. Because the fracture process zone characteristics are critical to material performance, a better understanding of those characteristics will lead to a better understanding of performance.

To investigate some of the microstructural phenomena that make up the fracture process zone, we conducted an experimental program using quantitative acoustic emission (AE) techniques. The specific goals of the program were to evaluate microcrack properties through the deconvolution of recorded AE waveforms and to examine the relationship between the recovered microcrack properties and the overall mechanical properties of the material. To this end, a series of plain (unreinforced) beam specimens were tested in three-point bending under closed-loop control. The microcracking was monitored using an array of AE transducers. The results of these experiments are presented in this paper.

Background

AE monitoring is a nondestructive test method for evaluating damage growth in structures. An AE is the spontaneous release of localized strain energy in a material. This energy release causes the propagation of stress waves that can be detected at the surface of the material. AEs result from microcracking, dislocation movement, phase transformations, and other irreversible changes. Through an analysis of detected AE waveforms, the nature of damage in the material can be deduced. AEs are typically monitored using highly sensitive piezoelectric transducers connected to some type of data recording device.

Analysis of AE phenomena can range from relatively simple counting of AE events, energy, or frequency analysis and locating AE sources [1] to the more sophisticated quantitative AE analysis [2]. Details of the types of analysis performed in this investigation are described later.

AE techniques have been applied to concrete for a number of years [3–6]. Diederichs et al. [6] compiled a

---

Address correspondence to: Eric N. Landis, Department of Civil and Environmental Engineering, University of Maine, 5711 Boardman Hall, Orono, Maine, 04469-5711.

Received May 27, 1994; Accepted December 5, 1994

655 Avenue of the Americas, New York, NY 10010

ISSN 1065-7355/95/$9.50
SSDI 1065-7355(95)00003-A

particularly extensive review of conventional AE applications to concrete. Included in their review are the effects of loading devices, specimen size, aggregates, ultimate strength, and temperature on the AE counts and frequency spectra. More recent work has focused on relating acoustic emission characteristics to properties of the fracture process zone [7–10]. AE source location analysis has also been applied to damage localization [11] as well as crack-tip measurements [12] in concrete. Quantitative AE analysis has been used to evaluate cracking due to anchor bolt pull-out [13]. The strength of AE measurement techniques is the ability to monitor microscopic damage occurring inside the material.

Traditional analysis of AE data involves the recording of event rates, peak amplitudes, frequency spectra, and source locations. Empirical relationships can be made with damage growth or other observed phenomena. Although this type of analysis can provide valuable insight into fracture behavior, a more sophisticated analysis is necessary for characterization of the actual microfracture event that caused the AE. Hsu et al. [2] established a quantitative acoustic emission model where the AE event is broken down into three separate processes: (1) the source (microcrack) event, (2) the resulting stress wave propagation through the material, and (3) the measurement of the waveform on the specimen surface. These three processes are assumed to be linear systems so that they may be combined through a series of convolutions as [14]:

$$V(t) = T(t)*\{G(t)*M(t)\} \tag{1}$$

where $V(t)$ is the voltage measured from an AE transducer, $M(t)$ is a function representing the AE source, $G(t)$ accounts for the wave propagation through the material, and $T(t)$ is the response function of the AE transducer. A separate response function for the transducer is necessary because the conversion of mechanical energy to an electrical signal is imperfect and must be taken into account. The asterisk denotes a convolution integral. Through an inverse analysis, the characteristics of an AE source can be determined from the measured voltage transients, if the response of the transducer and the wave propagation characteristics of the material are known.

Representation of an AE source can be accomplished through seismological equivalence models for earthquake faults. (It should be noted that AEs are often referred to as microseismic events.) A discontinuity in an elastic medium can be represented by an equivalent set of body forces that produce the same far field displacements as would the formation of a microcrack. This set of body forces is referred to as a seismic moment tensor and may be written in terms of the discontinuity as [15]:

$$M_{ij} = C_{ijkl} b_k n_l \Delta A \tag{2}$$

Here $b_k n_l \Delta A$ is discontinuity with area ΔA and slip direction (Burgers vector) b_k. The plane of the discontinuity has a normal vector n_l. C_{ijkl} is the elastic stiffness tensor, and M_{ij} is the seismic moment tensor. Since eq 2 represents an equivalence between the moment tensor and a discontinuity, any microcrack can be uniquely defined by the appropriate moment tensor components.

The characteristics of the microcrack may be determined from the moment tensor as follows [16]. For isotropic materials, eq 2 can be simplified to:

$$M_{ij} = [\lambda b_k n_k \delta_{ij} + \mu\,(b_i n_j + b_j n_i)]\Delta A \tag{3}$$

where λ and μ are the Lamé constants. The principal values (eigenvalues) of M_{ij} are governed by the equation:

$$(M_{ij} - M\delta_{ij})x_j = 0 \tag{4}$$

where M is a principal value, x_j is the corresponding principal direction (eigenvector), and δ_{ij} is the Kronecker delta. A nontrivial solution for eq 4 exists only if the determinant vanishes, or:

$$|M_{ij} - M\delta_{ij}| = 0. \tag{5}$$

Equation 5 leads to a cubic equation that yields three principal values. These values are:

$$M^{(1)} = [(\lambda + \mu)b_k n_k + \mu(b_k b_k)^{1/2}]\Delta A \tag{6a}$$

$$M^{(2)} = \lambda b_k n_k \Delta A \tag{6b}$$

$$M^{(3)} = [(\lambda + \mu)b_k n_k - \mu(b_k b_k)^{1/2}]\Delta A \tag{6c}$$

The three corresponding principal directions are:

$$x_i^{(1)} = b_i + n_i(b_k b_k)^{1/2} \tag{7a}$$

$$x_i^{(2)} = \epsilon_{ijk} b_j n_k \tag{7b}$$

$$x_i^{(3)} = b_i - n_i(b_k b_k)^{1/2} \tag{7c}$$

where ϵ_{ijk} is the permutation symbol.

These equations show that the vector, $\mathbf{x}^{(2)}$ is in the direction normal to the plane given by **b** and **n.** Equations 7a and 7c indicate that $\mathbf{x}^{(1)}$ is a vector on the plane defined by **b** and **n** in the direction that bisects the angle between them, and $\mathbf{x}^{(3)}$ is on the plane defined by **b** and **n**, and is normal to $\mathbf{x}^{(1)}$. These are illustrated in Figure 1.

Using the principal values and principal directions of the moment tensor, the microcrack can be characterized in terms of its orientation, volume, and slip direction.

The orientation is described by the direction of the crack plane normal vector **n**, which is defined by:

$$n_i = \frac{1}{2(b_k b_k)^{1/2}} (x_i^{(1)} - x_i^{(3)}) \tag{8}$$

The volume is evaluated in terms of the principal moment tensor values:

$$\Delta V = b_k n_k \Delta A = \frac{M^{(1)} + M^{(2)} + M^{(3)}}{3\lambda + 2\mu} \tag{9}$$

The direction of microcrack slip may be expressed as an angle between **b** and **n**. If this angle is designated at α, then:

$$\cos \alpha = \frac{b_k n_k}{(b_k b_k)^{1/2}} = \frac{2\mu M^{(2)}}{\lambda(M^{(1)} - M^{(3)})} \tag{10}$$

Using this designation, and angle of α close to 0° indicates mode I (tensile) microcracking, whereas an angle of α close to 90° indicates mode II (shear) microcracking. It should be noted that the convention used for the principal values was: $M^{(1)} > M^2 > M^3$.

Thus, through the use of eq 8–10, a microcrack may be uniquely characterized in terms of its volume, orientation, and slip angle. These parameters are determined from the principal values and directions of the moment tensor.

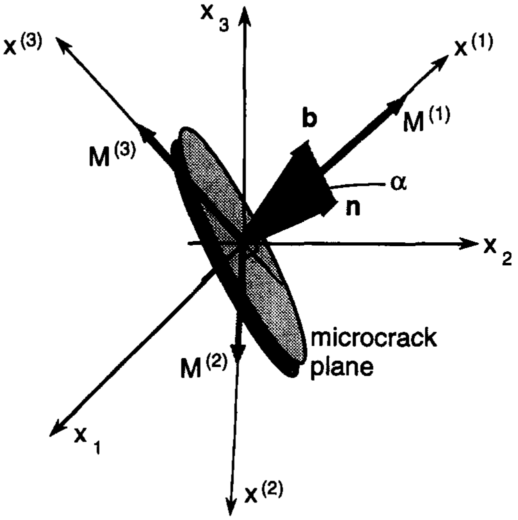

FIGURE 1. Orientation of principal axes relative to microcrack.

The moment tensor components are determined through an inversion of eq 1. The theoretical basis for eq 1 is an integral solution of the differential equation of motion in an elastic solid. The far field displacement u_i, in an elastic medium at point **x**, due to a transient body force f_j, acting at point ξ can be written [14]:

$$u_i(\mathbf{x},t) = \int_{-\infty}^{\infty} G_{ij}(\mathbf{x},\xi,t - \tau) f_j(\xi,\tau) d\tau \tag{11}$$

where G_{ij} is the elastodynamic Green's function for the medium. Because eq 11 is a convolution integral, G_{ij} may be thought of as the response of the medium at **x**, due to an impulse load (both spatial and temporal) applied at ξ. If the point force f_j, is replaced in eq 11 by a moment tensor source, M_{ij}, the equation becomes:

$$u_i(\mathbf{x},t) = \int_{-\infty}^{\infty} G_{ij,k}(\mathbf{x},\xi,t - \tau) M_{jk}(\xi,\tau) d\tau \tag{12}$$

where $G_{ij,k} = \partial G_{ij}/\partial x_k$ is the displacement response to a dipole source and is often referred to as a Green's function of the second kind. If eq 12 is convolved with the impulse response function for the AE transducer, the result is eq 1. Thus, if the Green's function for the medium and the transducer response function are known, then moment tensor representing a microcrack can be determined through an inversion of eq 12. This inversion can be somewhat difficult. A detailed description of the inversion procedure used in this study is presented in ref 17. The procedure may be summarized as follows. For a particular AE event, an array of transducers measures the resulting stress wave transients. The voltage transient measured at each transducer is deconvolved with the impulse response of the transducer. This deconvolution leads to the surface displacement transient at the location of the transducer. These displacements represent the left-hand side of eq 12. Because the moment tensor has six independent components, a minimum of six channels of data is required. A Green's function for an infinite medium was used in eq 12 with a correction for mode conversion at the specimen boundary [18]. A nonlinear least-squares approach was developed for the required multichannel inversion. The multichannel inversion produces the nine moment tensor components. The moment tensor is then rotated to its principal axes using eq 4. Finally, the principal values and directions are used in eqs 8–10 to evaluate the microcrack parameters of volume, slip, and orientation.

Before the test, the location and response functions for all transducers must be known. The response functions are determined through calibration against a known reference signal [19]. Also, the elastic properties (Lamé constants) of the specimen must be known for evaluating the Green's function for the material. Because the elastic constants govern the wave propagation through the material, dynamic measurements of these constants are better suited than static measurements. The dynamic elastic moduli for a material can be evaluated through measurements of the longitudinal (P-wave) and transverse (S-wave) wave velocities and the mass density of the material [20].

The inversion procedure was found to be fairly robust and was verified using redundant measurements [17]. With this measurement and analysis system in place, the technique could then be applied to basic problems of fracture in cement based materials.

Experimental Program

An experimental program was carried out to examine the relationship between the microfracture characteristics and the overall mechanical response of the material. To make this examination, we tested specimens of different microstructural characteristics. The properties of the specimens as well as the types of tests conducted as described below.

Specimen Properties

A series of three-point bend specimens of varying composition were cast for this program. The specimens were designated as follows: coarse mortar, fine mortar, plain cement paste, and densified using small particles (DSP) cement paste. The composition of each specimen tested is summarized in Table 1. The results of previous experiments showed that a coarse mortar represents the practical limit of quantitative AE analysis of microcracking in cement based materials [21]. The proportion of aggregate in the mortars was 2 parts aggregate to 1 part cement. The mortars and the cement paste are fairly common materials for laboratory analysis, and the specimen fabrication was conducted using the relevant ASTM guidelines (e.g., ASTM C 192-81, *Making and Curing Concrete Test Specimens in the Laboratory*). DSP cement paste requires additional description as there is no standard for its fabrication.

TABLE 1. Composition of tested specimens

Material	Maximum Aggregate Size	Water: Cement Ratio	Specimen Size
Coarse mortar	5 mm	0.45	large
Fine motar	1 mm	0.45	large
Normal cement paste	—	0.45	large and small
DSP cement paste	—	0.20*	small

*Water:solid ratio; 18% silica fume added.

DSP cement paste is a portland cement based material with a very low water:cement ratio and a relatively large fraction of added silica fume. Because of the small amount of water, a superplasticizer is required. After the constituents are thoroughly mixed, a vacuum is applied to minimize the amount of air in the pores. The result is a material with a very dense microstructure (as compared with conventional cement based materials). This dense microstructure leads to a large increase in strength compared with normal cement paste.

All of the specimens were demolded approximately 24 hours after loading and were placed in a water bath for curing.

Two different sized specimens were tested. The specific specimen geometries are shown in Figure 2. Three large specimens were tested: coarse mortar, fine mortar, and normal cement paste. Two small specimens were tested: DSP paste and normal cement paste. The smaller size was chosen for the DSP specimen because of the difficulty in properly casting large DSP specimens. A small normal cement paste specimen was also tested so that there would be a common reference for both sizes, eliminating any possible size-related bias in the measurement system.

Specimen Loading

All specimens were tested in a closed-loop, servo-hydraulic load frame. The experimental set-up is illustrated in Figure 3. The closed-loop feedback parameter for the large specimens was the tensile strain as measured by a 4-inch extensometer mounted on the bottom of the beam. For the small specimens, a center notch was cut in the beams and a gauge was placed over the notch for crack mouth opening displacement (CMOD) measurements. The CMOD measurement was used as the feedback control. The absence of a notch in the large specimens allowed the localization of microcracking to be observed. When a notch is added to the specimen, formation of the critical crack is confined to the area of the notch. Because the location of the critical crack is known, a much finer gauge can be used to monitor crack growth, and thus much better control of the loading in the postpeak region can be maintained. Because the mechanical properties of DSP pastes have not been extensively studied, CMOD control was used in this test to ensure stable crack growth.

It should be noted that differences between these two control modes occur only in the prepeak loading stage. Once a critical crack forms, the two modes are essentially the same. That is, after the formation of a critical crack, nearly all subsequent opening of the extensometer is due to crack opening rather than elastic

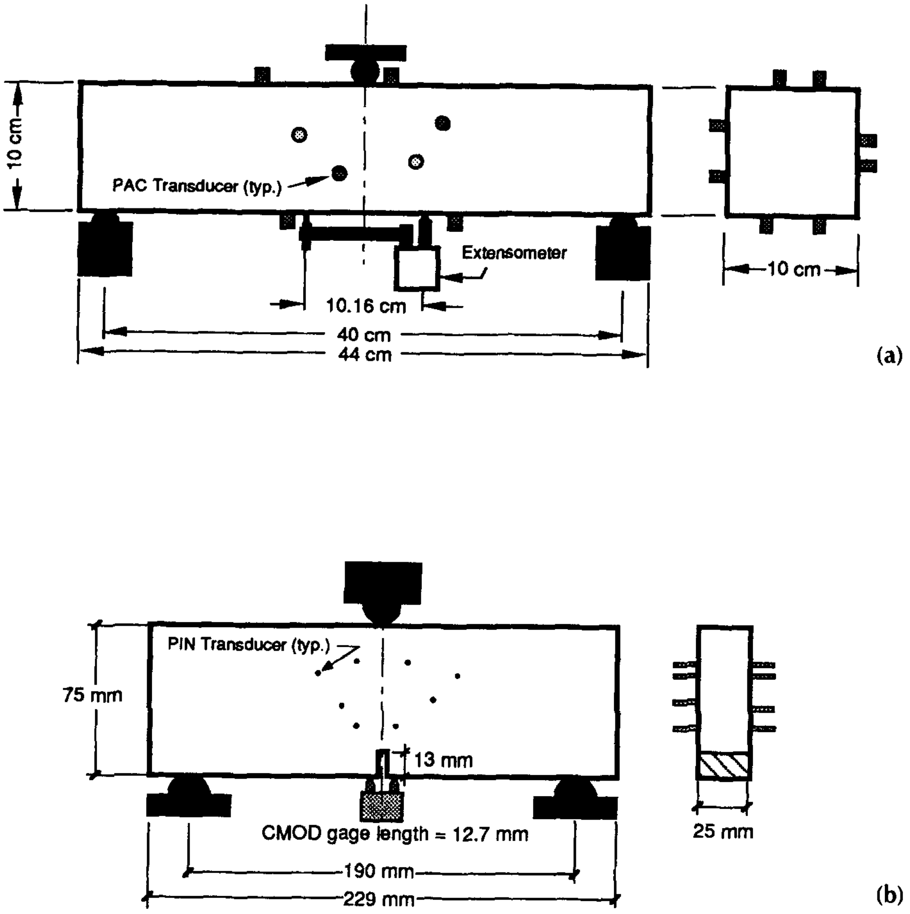

FIGURE 2. Geometries of specimens tested: (a) large unnotched specimen and (b) small notched specimen.

deformation. The output of the 4-inch extensometer thus becomes a measurement of CMOD, and the differences between the two gauges is only a function of their respective gauge lengths.

The specimen loading rate was programmed such that the displacement gauges would open at a rate of 5.0×10^{-5} mm per second for the large specimens and 3.5×10^{-5} mm per second for the small specimens.

Measurement System

The components of the AE measurement system are illustrated in Figure 3. A LeCroy modular transient recorder system was used to acquire the AE waveforms. A LabVIEW-based application was developed to record the signals and to control the LeCroy system. For all tests, eight channels of AE data were recorded. The length of the data record for each channel was 1,024 points. The sampling rate of the transient recorders was 16 MHz for the large specimens and 32 MHz for the small specimens.

Two different types of piezoelectric transducers were used: the model micro80 AE transducer manufactured by Physical Acoustics Corp (PAC), and the model CA-1135 position transducer (PIN) manufac-

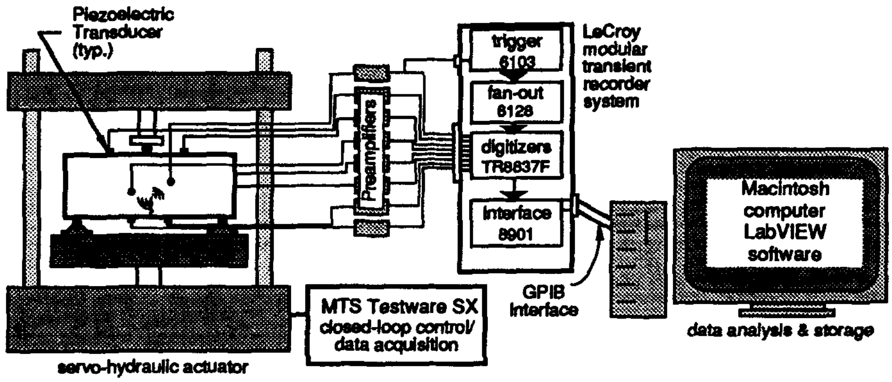

FIGURE 3. Experimental test set-up.

tured by Dynasen Inc. Each of the transducers was calibrated against a glass capillary reference signal [19]. The PIN transducers were found to have a more broadbanded displacement response than the PAC transducers. However, the PAC transducers were much more sensitive up to about 250 kHz [21]. The PINs were initially chosen for use in all experiments, but it was soon discovered that they were not sensitive enough to detect many of the AE events in the large specimens. Therefore, the PAC transducers had to be used for the large specimens. It was found that PINs were sensitive enough to detect a large number of AE events in the small specimens, so they were used for those tests.

The output of each transducer was amplified by Physical Acoustics model 1220B preamplifiers. Pretest calibrations were performed for each channel so that the measured voltage transients for each AE event could be converted to a series displacement transients using a time domain deconvolution procedure [17].

Experimental Results

The results of five different experiments are reported in this section. The five tests are as follows: large geometry specimens of normal cement paste, fine mortar, and coarse mortar, and small geometry specimens of DSP cement paste and normal cement paste. The compositions and measured elastic properties of these specimens are shown in Tables 1 and 2, respectively.

Although two different specimen sizes were used along with two different types of AE transducers, the results of the analysis should not be affected by either measurement system or specimen geometry. As an experimental check, however, a large paste specimen was tested in order that there be overlap between the two configurations. Unfortunately, large shrinkage cracks developed in the large paste specimen such that the overall behavior was not representative of that material. The peak load was a fraction of what it should have been for that material, and only a limited number of AE events were recorded. The results that follow thus focus primarily on the four remaining tests. Where appropriate, the results from the large paste specimen are also included.

Load and AE Event Data

The cumulative AE event counts are plotted along with the loads for four specimens in Figure 4. It should be noted that the event count shown here is heavily influenced by the recording rate of the data acquisition system and the sensitivity of the transducers. Because whole waveforms were recorded for each event, the maximum rate that the data acquisition system could record the AE signals was approximately three events per second. It is likely that there is more AE activity that is not recorded during the downtime of the acquisition system. (The acquisition system cannot record new signals while the previous event is being saved.) Thus, the event numbers shown here cannot necessarily be compared with the counts typically acquired by conventional AE monitoring equipment.

The event rates shown in Figure 4b–d illustrate an interesting characteristic of the AE properties of cement based materials. This characteristic is that the rate of AE activity appears to increase just prior to the ultimate load. In the fine mortar specimen, the increase in event rate occurs at about 75% of the peak load. The specimen also shows typical nonlinear prepeak behavior. In the DSP specimen, the event rate jump occurs at about 86% of the peak. There is also a notable nonlinear prepeak region in this specimen. These can be contrasted with the small paste specimen where the prepeak portion of the load curve is essentially linear right up to the peak load. The jump in the AE event rate occurs at the peak load as well.

Li and Shah [11] attributed this jump in the AE event rate to the localization of microcracking into a single critical crack. In their specimens of mortar and concrete, the jump occurred typically at about 80% of the peak load. Ohtsu [22] attributed the AE event rate increase to the formation of the fracture process zone. He also suggested that a linear elastic fracture mechanics (LEFM) approach could be applied to concrete if the load for evaluating fracture toughness was taken as the load where the AE event rate jumps and the fracture process zone forms.

TABLE 2. Measured elastic properties of tested specimens

Material	P-wave Velocity	S-wave Velocity	Lamé Constants		Attenuation (at 100 kHz)
			μ	λ	
Coarse mortar	4330 m/s	2540 m/s	14.4 GPa	13.1 GPa	−0.20 dB/mm
Fine mortar	3930 m/s	2500 m/s	13.6 GPa	6.39 GPa	−0.15 dB/mm
Normal cement paste	3500 m/s	1940 m/s	7.49 GPa	9.40 GPa	−0.08 dB/mm
DSP cement paste	4620 m/s	2580 m/s	1.52 GPa	18.4 GPa	−0.05 dB/mm

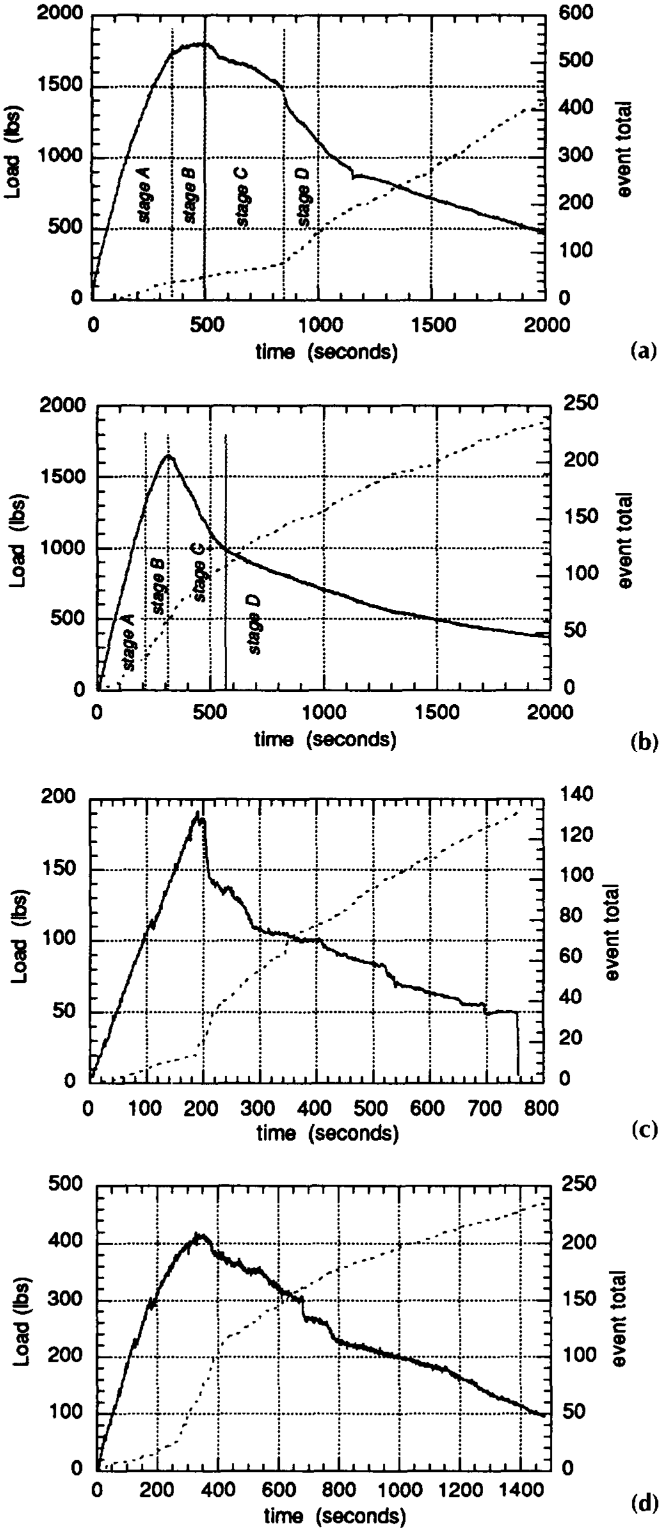

FIGURE 4. Load and cumulative event counts: (a) coarse mortar specimen, (b) fine mortar specimen, (c) normal cement paste specimen, and (d) DSP cement paste specimen.

The exception to these observations is with the coarse mortar specimen. For some reason the event rate does not jump until well into the postpeak region. The jump in event rate in this specimen does seem to correspond to some physical phenomenon. Specifically, the event rate jumps at a point where the load capacity of the beam drops dramatically. This is considered further in the Discussion section.

In Figure 4a and b, four loading stages are labeled as stage A through stage D. The four stages refer respectively to (1) the linear prepeak region; (2) the prepeak nonlinear region (after localization); (3) the initial postpeak region; and (4) terminal postpeak region. These regions are further addressed in the following discussion.

AE Source Locations and Localization

The locations of the AE sources were evaluated according to the methods described in ref [23]. Based on the arrival times of the first P-wave at each transducer and the respective P-wave velocities in each material, the source locations for all measurable events were evaluated. The definition of a measurable event was one that had a minimum of four well-defined arrival times. In general, if at least four arrival times were fairly well defined, then the event location was evaluated with a relatively high degree of certainty.

The accuracy of the source locations was estimated by applying an artificial source (pencil lead fracture) at a known location on the specimens. The locations of the sources were evaluated using the AE source location routines and the result was compared with the actual location. Based on this analysis, the location resolution of each specimen was estimated to be the following: coarse mortar, ±5 mm; fine mortar, ±2 mm; normal cement paste, ±1 mm; and DSP cement paste, ±1 mm.

The likely reason for the poorer resolution of the coarse mortar is the slight variation of P-wave velocity in the specimen. Variations in wave propagation velocity may arise based on the number of aggregate crossings over the path of wave propagation. For this analysis, the P-wave velocity was assumed to be a constant for the analysis of AE source locations event though there may be some variability depending on the wave propagation path.

Some comments on the estimated source locations follow.

COARSE MORTAR SPECIMEN. The source locations evaluated in the coarse mortar specimen are shown at four different stages in Figure 5. The first figure shows the AE events located during the initial stages in the loading cycle. This corresponds to the essentially linear portion

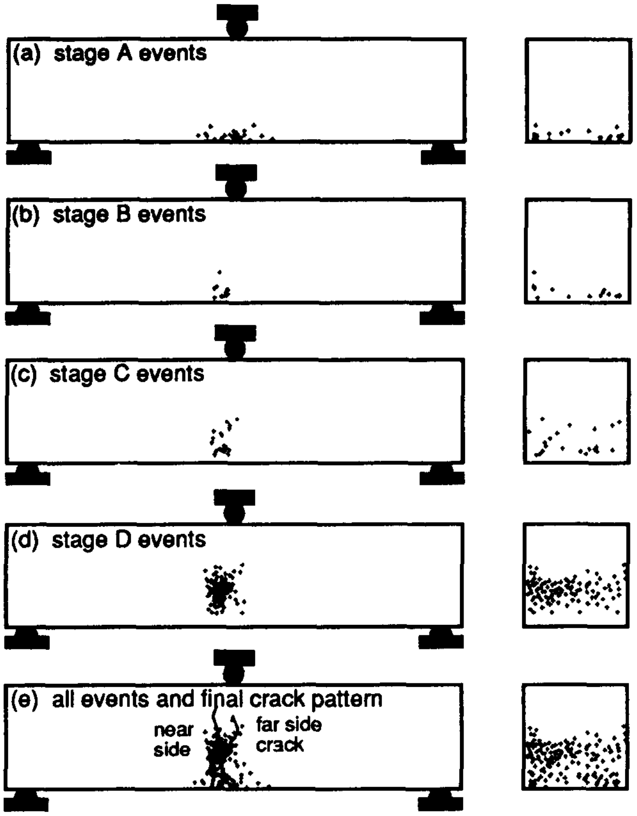

FIGURE 5. Acoustic emission source locations in coarse mortar specimen.

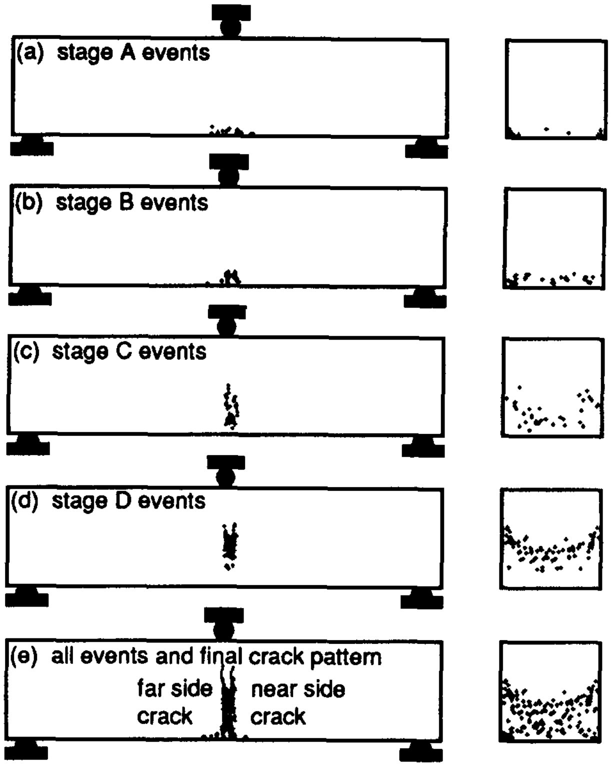

FIGURE 6. Acoustic emission source locations in fine mortar specimen.

of the load-strain curve of Figure 4a. As can be seen in Figure 5, the AE events were fairly evenly distributed throughout the zone of maximum tensile stress in the specimen. The second set of event locations shown corresponds to the segment of the load-strain curve where slope changes significantly. The AE events occurring during this time were confined to a narrow band just to the left of the beam centerline.

The remaining two segments shown in Figure 5 correspond to the initial postpeak region and the region of steady-state crack growth, respectively. The distinguishing characteristic that separates these two segments is not in the source location plots but rather is in the cumulative event count plot in Figure 4a. At about 78% of the peak load (postpeak), the event rate jumped dramatically. There does not seem to be an explanation for this jump in the location plots; however, additional information from the quantitative analysis provided some insight into this behavior. This is described in the Discussion section.

FINE MORTAR SPECIMEN. The source locations evaluated in the fine mortar specimen are shown at four different stages in Figure 6. As with the coarse mortar specimen, the initial events were somewhat evenly distributed along the zone of maximum tensile stress. In this specimen, there was a distinct jump in the event rate at about 75% of the peak load. The AE events located after this rate jump are confined to a narrow band that ultimately corresponded to the location of the main visible crack. The events located during the postpeak portion of the load-strain curve are also concentrated along this narrow band. Again, this localization and corresponding jump in event rate agrees quite well with the results of Li and Shah [11].

An examination of the AE event locations viewed in the beam's cross section leads to some interesting observations. The AE events in the initial stage of loading seem to be confined to the corners of the specimen. It would seem from this that damage is initiated along the sides of the specimen. As the loading cycle progresses and the event locations move up the cross section, this trend continues. It is most clearly seen during the fourth stage. The events are further up the cross section at the sides than they are in the center. This phenomenon was also observed by others using a dye penetration technique [24]. Although the exact cause is not clearly understood, it is likely that the occurrence of small shrinkage cracks at the corners cause cracks to initiate there.

There are some interesting differences between the source location results of the fine and coarse mortar specimens. First, the scatter of AE events in the coarse mortar is much larger than in the fine mortar. This is particularly apparent in the plots of all events. Part of the extra scatter in the coarse mortar can be directly attributed to the lower resolution of the source location routine for that material. However, it is also likely that the fracture processes in the coarse mortar also contribute to a wider scatter. It can be seen in the crack patterns shown in Figures 5e and 6e that the critical crack propagates in a more obtuse angle through the cross section in the coarse mortar specimen. This accounts for some of the scatter as viewed from the side. In addition to the path of the critical crack, it is likely that some of the scatter can be attributed to fracture processes, such as microcracking, that surround but are not directly connected to the main crack. It is this wider distribution of microcracking observed in the coarse mortar specimen that likely leads to the overall increase in toughness as discussed later.

AE source locations were also evaluated for the normal and DSP paste specimens. In both cases, the AE sources moved up from the precut notch in a narrow band about 3-mm wide, with relative uniformity through the thickness of the specimen.

Characterization of Microcracking

The quantitative AE model used in this series of experiments was previously described. A seismic moment tensor is used to represent the microcrack source, a Green's function solution for an infinite medium with a correction for the boundary effects was used to model the stress wave propagation through the medium, and the impulse response of the transducers was evaluated by pretest calibration experiments. These three terms are related by a series of convolutions as shown in eq 1. An iterative approach was previously developed to evaluate the moment tensor components [17]. The moment tensor components are then used to characterize the microcrack properties.

For the analysis presented here, an additional term was added to the quantitative AE model. Based on preliminary studies of ultrasonic attenuation in cement based materials, we found that materials of different composition and degree of inhomogeneity showed different attenuation characteristics [25]. In order that these attenuation effects would not influence the results of the quantitative AE analysis, an attenuation term was added to eq 1. The model can then be written as:

$$V(t) = T(t)*\{[G(t)*M(t)]\bar{\alpha}\} \tag{13}$$

where, as previously mentioned, $M(t)$ is a function representing the AE source, $G(t)$ is the appropriate elastodynamic Green's function for the material, $T(t)$ is the impulse response of the AE transducer, and $V(t)$ is the output of that transducer. An asterisk denotes convolution. $\bar{\alpha}$ is the total material attenuation that occurs as the AE wave passes from the source to the receiver. Its value is a function of the material attenuation coefficient, α, and the source receiver separation distance, L:

$$\bar{\alpha} = 10^{(\alpha L/20)} \tag{14}$$

It is assumed that attenuation is essentially frequency independent (constant) over the frequency range of analysis. The attenuation coefficient, α, for the materials tested are shown in Table 2. A point source/point receiver ultrasonic technique was used to measure α [26].

The steps in the analysis process are briefly summarized here. Details are presented in ref 21. All of the analysis takes place after the test.

For a particular AE event, waveforms from all eight channels are examined. The wave arrival times are evaluated for all signals of sufficient amplitude. If a minimum of four signals had sufficient amplitude, then the location of the AE event was calculated. If the event had a minimum of six signals of sufficient amplitude, then the moment tensor was also evaluated. This calculation first requires that the measured voltage transients be converted to a displacement transient through the deconvolution with the transducers' impulse response functions. These impulse response functions were evaluated before the tests using the calibration methods described in ref 19. The displacement transients are then used to iteratively estimate the six independent components of the moment tensor. Once the moment tensor was recovered for a particular event, then the microcrack parameters such as volume, slip angle, and crack plane orientation were calculated using the equations presented earlier.

The recovered microcrack volumes were calculated for each specimen and are plotted in Figure 7. There does not appear to be any tremendous differences between the various materials. The microcracks in the mortars tend to be mostly in the range of 10,000 μm^3, whereas the paste specimens tend to have more cracks in the range of 20,000 μm^3. The volumes recovered are a measure of the energy release of the microcrack, because it is a function of the principal moment tensor values and the elastic properties. It is not, however, necessarily a good indication of the area or opening of a microcrack, because these values are indeterminate.

The recovered slip angles for each specimen are shown in Figure 8. The slip angle, α, was defined as the angle between a vector normal to the microcrack plane and a vector representing the direction of crack motion of one face relative to the other. Using this definition, a slip angle close to 0° indicates mode I (tensile) microfracture, whereas a slip angle close to 90° indicates mode II (shear) microfracture. Angles in be-

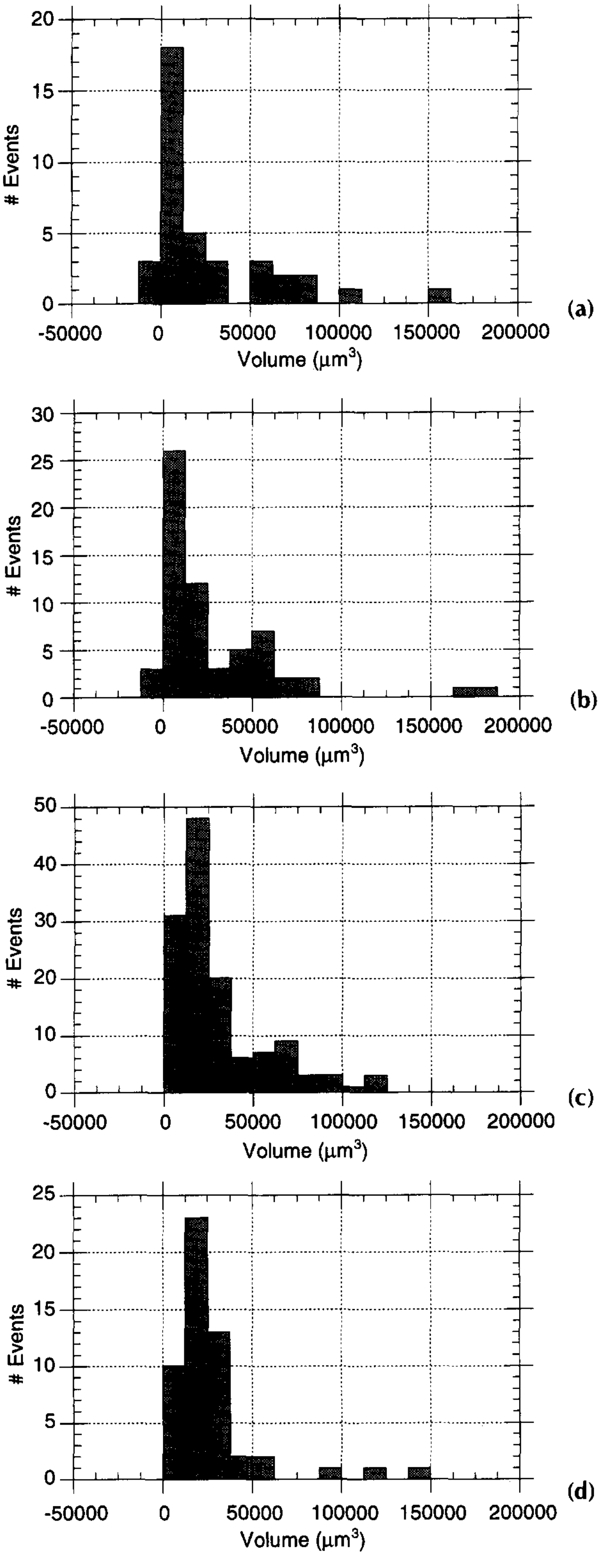

FIGURE 7. Histogram of microcrack volumes: (a) coarse mortar specimen, (b) fine mortar specimen, (c) normal cement paste specimen, and (d) DSP cement paste specimen.

tween are mixed mode. The majority of the microcrack slip angles recovered for the two mortar specimens tend to be relatively close to 90°, indicating a dominance of shear fracture modes. There is a significant difference in the slip angles of the paste specimens. Both show much larger crack opening components (smaller slip angles). Although the shear component in both of these is still fairly high (a majority of normal paste events had slip angles in the 70° to 75° range whereas the DSP had the most events in the 65° to 70° range), it seems clear that the nature of the microcracking is different in the fine-grained versus the coarse-grained materials.

Discussion

A goal of this research program was to examine the relationship of the AE analysis results with overall mechanical properties of the different materials. The particular properties discussed here are the localization of microcracking, the variations in microcrack characteristics during the loading cycle, and fracture toughness and fracture surface roughness.

Localization

Figures 5 and 6 illustrate the notion of damage localization in the materials. Initially, microcracks form in a somewhat random pattern in the zone of maximum tensile stress. Then at some point, the microcracks coalesce into an area around the location of the critical (continuous) macrocrack. The progression of microcracking into the narrow band explains the increasingly nonlinear (decreasing stiffness) prepeak stress-strain behavior. This progression can also be observed using laser interferometry techniques [27].

Although the AE source locations in the notched specimens were confined to a narrow band extending from the notch tip (no visible localization), it would seem from the analysis of the AE data that the concept of localization is not confined to unnotched specimens. Localization appears to occur in the notched specimens as well.The difference between the two types of specimens is that the location of the critical macrocrack is unknown in the unnotched specimens whereas the addition of the notch forces the critical crack to extend from the notch tip. It is apparent from the data here that if localization is defined as the coalescence of microcracks into a macrocrack, then localization also takes place in the notched specimens. Evidence of this is mainly in the jump in event rate that tends to accompany localization. Both of the notched specimens tested here showed a jump in the event rate before the peak load. In each case, this jump in AE event rate accompanies nonlinearities in the ascending portion of

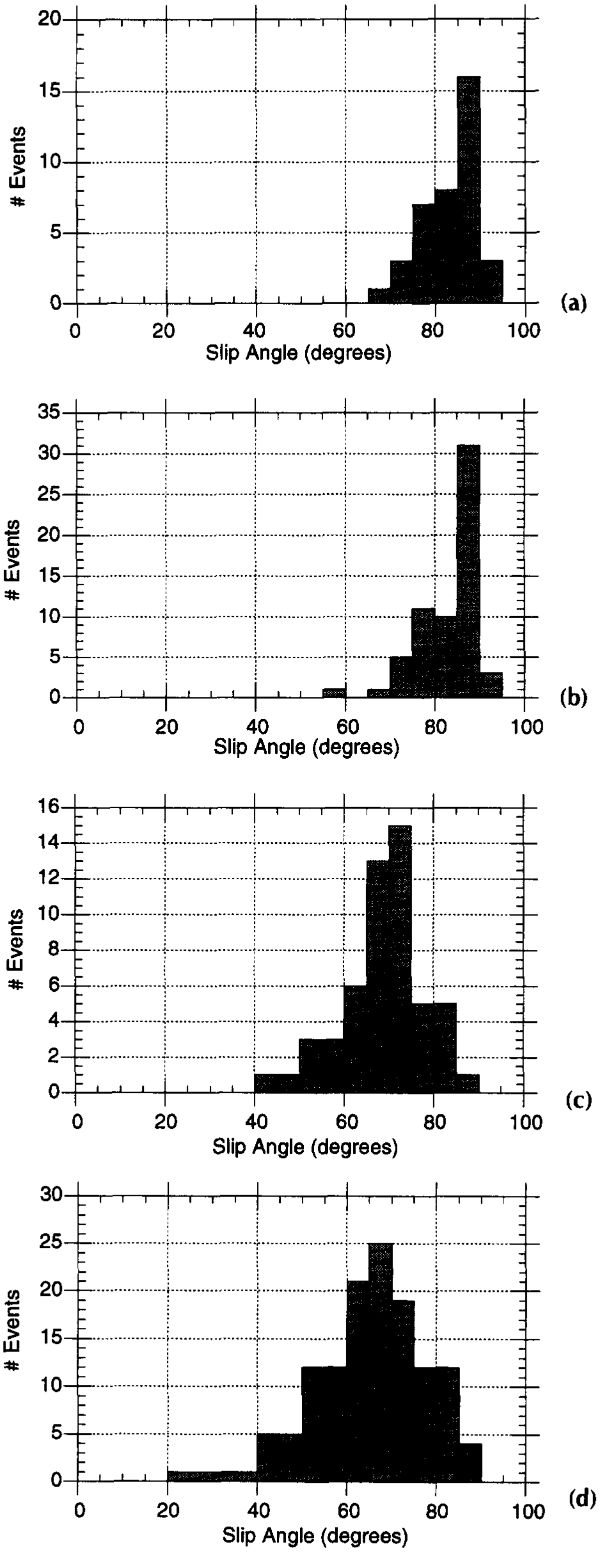

FIGURE 8. Histogram of slip angles: (a) coarse mortar specimen, (b) fine mortar specimen, (c) normal cement paste specimen, and (d) DSP cement paste specimen.

the load-CMOD curves. It may be concluded that localization has less to do with where a macrocrack forms than in how it forms.

Progression of Microcracking

It was previously pointed out that the there was not a jump in the AE event rate corresponding to localization in the coarse mortar specimen. There was a jump in the event rate later in the test, but it could not have anything to do with localization because it occurred well into the postpeak region of the load-strain curve as shown in Figure 4a. A quantitative AE analysis of microcracking in the specimen showed that the jump in AE event rate may have corresponded to a shift in the characteristics of the microfracture.

A plot of the recovered microcrack volumes and the corresponding load are shown in Figure 9. It can be seen in the figure that at the point where the AE event rate jumped (at the same time as a sudden drop in the load), the volumes tend to be smaller. That is, at the point where microcracks start occurring at a higher rate, they also become smaller. This could indicate a shift in the dominant mechanism of microfracture. This shift can also be seen in a similar plot that shows load and microcrack slip angle (Figure 10). At roughly the same time as the drop in microcrack volume, there is also a jump in slip angle. This indicates a move towards a shear dominated microfracture mode.

The characteristics shown in Figures 9 and 10 could represent microcracking in different material phases. Microcracks occurring early in the loading cycle have been attributed to primarily matrix-aggregate interface cracks. As load approaches the peak, the microcracking also includes the matrix phase [28]. If it is assumed that matrix cracking consists of a higher energy release than interface cracking, then Figure 9 shows that there is primarily matrix cracking around the peak load,

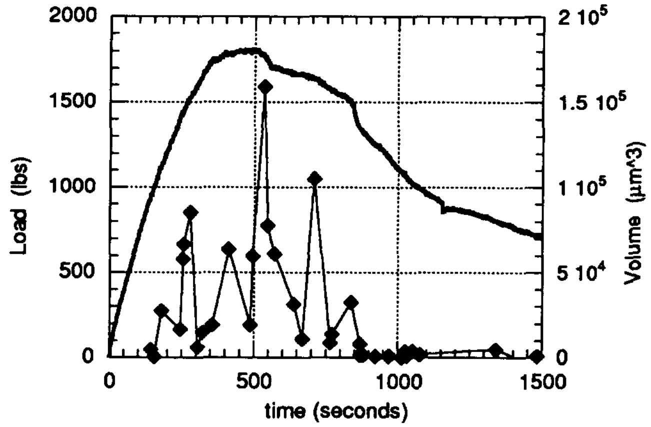

FIGURE 9. Load and volume histories for coarse mortar specimen.

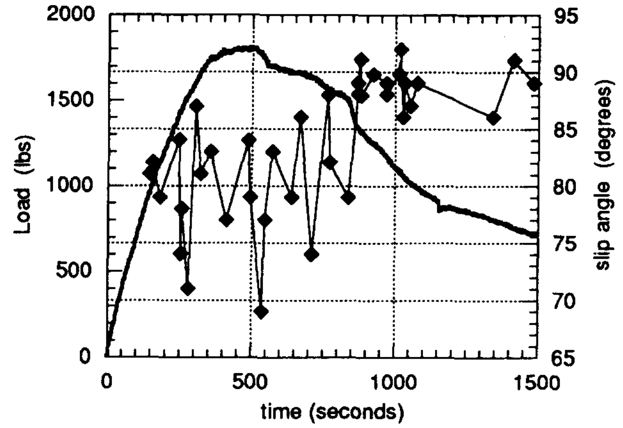

FIGURE 10. Load and slip angle history for coarse mortar specimen.

whereas the strain softening region could primarily be interface cracking. If this is the case, then from Figure 10 it could be concluded that the matrix cracking is predominantly mixed mode, whereas the interface cracking is primarily shear. This idea could be confirmed by the dominant mode of microcracking (mixed mode) observed in both of the paste specimens.

Fracture Toughness

A property examined for correlation with the recovered microcrack properties was overall fracture toughness of the materials tested. Traditional fracture toughness, K_{IC}, computed using linear elastic fracture mechanics techniques is not applicable to cement based materials because of the various fracture process zone effects [29]. Therefore, a second parameter is added to fracture toughness to account for these toughening mechanisms. The second parameter is a critical crack-tip opening displacement ($CTOD_C$) calculated at the tip of an effective elastic crack. These parameters can be calculated from load-CMOD curves that include a loading and unloading cycle. An effective critical crack length is estimated from the differences in initial loading compliance and unloading compliance.

The RILEM standard [30] was used to evaluate fracture toughness. Tests on the DSP and cement paste specimens were conducted as a part of this experimental program. Fracture toughness values for the fine and coarse mortar specimens were taken from published tests of comparable materials [29]. The values of fracture parameters used in this analysis are shown in Table 3.

The microcrack parameter used for correlation with fracture properties was the slip angle, α. It was felt that this was the single parameter that distinguished the materials. In Figure 11, the critical effective crack length, a_c, is plotted against the average slip angle, α. The critical effective crack length is a function of both K_{IC} and $CTOD_C$, so it is probably the best single parameter for describing the fracture behavior of the material. (It should be noted that K_{IC} and $CTOD_C$ are defined as material properties that are independent of geometry. a_c, however, is geometry *dependent*, so it is only appropriate to compare these values for specimens of the same size and loading configuration.) As can be seen in the figure, there is clearly a relationship between α and a_c. Of course, there are not enough data points for any statistically significant relationship, but the trend is apparent.

Fracture Surface Roughness

Lange et al. [31] evaluated the fracture properties of a variety of cement based materials through a microscopic examination of fracture surfaces. Because the tortuosity and roughness of fracture surfaces in cement based materials are related to increases in fracture toughness, Lange et al. performed quantitative analyses of the crack faces so that comparisons could be made with mechanical properties. The parameter that was used to characterize the fracture surfaces was the roughness number, RN. RN is the ratio of the surface area of a particular segment of a crack face with the projection of that area on a plane. The larger the roughness number, the greater the degree of irregularity and tortuosity. Values of RN corresponding to the materials tested in this investigation are shown in Table 3. Figure 12 shows a plot of roughness number

TABLE 3. Values of fracture parameters of tested specimens

Material	K_{IC} (KPa $\sqrt{m}$)	$CTOD_c$ (mm)	a_c (mm)	RN*	Average slip angle, α (degrees)
Coarse mortar	703	.0046	21.6	2.78	83.3
Fine mortar	727	.0053	21.6	2.53	83.7
Normal cement paste	380	.0041	17.36	1.83	64.8, 66.1‡
DSP cement paste	717	.0033	17.09	1.85†	68.6

K_{IC} = fracture toughness; $CTOD_c$ = critical crack-tip opening displacement; a_c = critical effective crack length; RN = roughness number.
*From Lange et al. [29].
†This value is actually for a 10% silica fume cement paste.
‡The first value was calculated from the large paste specimen and the second from the small paste specimen.

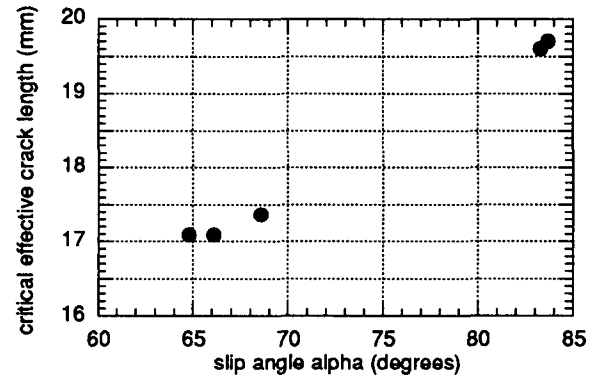

FIGURE 11. Critical effective crack length versus slip angle.

versus slip angle for the specimens tested. Again, despite the limited number of data points, there does seem to be a correlation between the roughness number and the microcrack slip angle.

A more recent analysis of fracture surface roughness [32] showed that the presence of the aggregate significantly affects the roughness of the cement matrix. The addition aggregate to otherwise similar matrix phases caused an increase in the fracture surface roughness near the aggregate. It was previously suggested [17] that microstructural features such as crack tortuosity, grain boundary sliding, and crack bridging could be responsible for the large number of shear-mode microcracking. The observation that the fracture surface roughness increases close to an aggregate relates well to the presumption made earlier that the matrix cracking tended to be mixed mode whereas interface cracking tends towards shear. The observed increase in crack tortuosity could clearly lend itself to a higher shear component in microfracture mode.

Conclusions

It is apparent from the results of this investigation that quantitative AE analysis yields a wealth of information about microcracking and fracture processes. The AE event rate, the source locations, and the microcrack parameters all can be synthesized to aid in the understanding of microcracking and its role in mechanical behavior. Increases in AE event rate were shown to correspond to localization of randomly distributed microcracks into a single damage zone. The AE source locations in the coarse mortar specimen showed significantly more scatter than the fine mortar, indicating a larger damage zone. The coarse mortar had a higher overall toughness, attesting to the fact that diffuse damage leads to greater energy absorption capacity. The microcracks were characterized according to their volume and slip angle using a seismic moment tensor model. Microcracks in the paste specimens were found to be primarily mixed-mode microfracture. Microcracks in the mortar specimens were found to have a large proportion of shear-mode microcracks. It was suggested that the shear microcracks in the mortars were primarily matrix-aggregate interface cracks, whereas the mixed-mode microcracks were in the cement matrix.

The relationship between microcrack slip angle and fracture toughness presented here illustrates how the properties of individual microcracks can affect the overall response of the material. Specifically, the addition of aggregate to the cement matrix causes a diffusion of damage (as shown in the location data) and a change in the microfracture mode in the vicinity of the aggregate. The shear microfracture mode could be the result of grain boundary sliding and other frictional mechanisms that absorb energy and increase toughness.

In summary, the results of the tests conducted as a part of this research program can be used to infer properties of the fracture process zone as well as the specific characteristics of individual microcracks. The properties of the microcracks can ultimately be linked to the mechanical behavior of the materials.

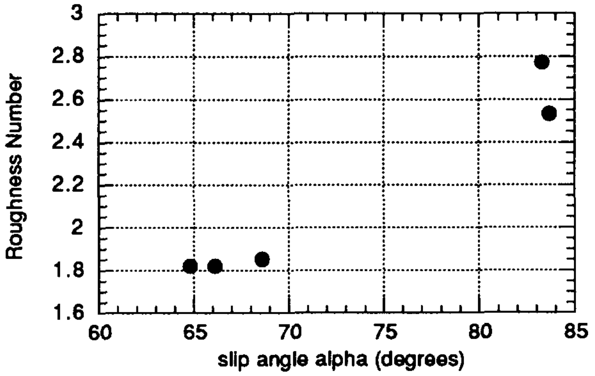

FIGURE 12. Roughness number versus slip angle.

Acknowledgments

The authors wish to acknowledge the support of the Air Force Office of Scientific Research and the program manager Dr. Spencer T. Wu, and the National Science Foundation Center for Advanced Cement-Based Materials at Northwestern University.

References

1. Miller, R.K.; McIntire, P., Eds. *Nondestructive Testing Handbook: Volume 5, Acoustic Emission Testing;* American Society for Nondestructive Testing Columbus, OH: 1987.
2. Hsu, N.N.; Simmons, J.A.; Hardy, S.C. *Mater. Eval.* **1977**, *35*, 100–106.

3. McCabe, W.M.; Koerner, R.M.; Lord, A.E. *ACI J.* **1976,** *73,* 367–371.
4. Nielson, J.; Griffin, D.F. *J. Testing Eval.* **1977,** *6,* 467–483.
5. Tanigawa, Y.; Yamada, K.; Kiriyama, S. *Trans. Jpn Concr. Inst.* **1980,** *2,* 155–162.
6. Diederichs, U.; Schneider, U.; Terrien, M. In *Fracture Mechanics of Concrete;* Wittman, F.H., Ed.; Elsevier Science Publishers B.V.: Amsterdam, 1983.
7. Maji, A.K.; Shah, S.P. *Exper. Mech.* **1988,** *28,* 27–33.
8. Rossi, P.; Robert, J.L.; Gervais, J.P.; Bruhat, D. *Matéiaux et Constructions* **1989,** *22,* 194–198.
9. Niiseki, S.; Mihashi, H.; Nomura, N. In *Progress in Acoustic Emission VI;* The Japanese Society for NDI, Tokyo; 1992; pp 463–470.
10. Maji, A.K.; Ouyang, C.; Shah, S.P. *J Mater. Res.* **1990,** *5,* 207–217.
11. Li, Z.; Shah, S.P. *ACI Mater. J.,* **1994,** *91,* 372–381.
12. Chen, H.L.; Cheng, C.T.; Chen, S.E. *Mater. Eval.* **1992,** *50,* 888–894.
13. Ohtsu, M.; Shigeishi, M.; Iwase, H.; Koyangi, W. *Mag. Concr. Res.* **1991,** *43,* 127–134.
14. Michaels, J.E.; Michaels, T.E.; Sachse, W. *Mater. Eval.* **1981,** *39,* 1032–1036.
15. Aki, K.; Richards, P.G. *Quantitative Seismology, Theory and Methods;* W.H. Freeman: New York, 1980; chap. 2–4.
16. Enoki, M.; Kishi, T. *Int. J. Fract.* **1988,** *38,* 295–310.
17. Landis, E.N.; Shah, S.P. *J. Nondestruct. Eval.* **1993,** *12,* 219–232.
18. Scruby, C.B.; Baldwin, G.R.; Stacy, K.A. *Int. J. Fract.* **1985,** *28,* 201–222.
19. *Annual Book of ASTM Standards, Vol. 03.03,* ASTM E1106-86; ASTM: Philadelphia, 1986; pp 949–969.
20. Kolsky, H. *Stress Waves in Solids;* Dover: New York, 1963.
21. Landis, E.N. *Ph.D. Dissertation;* Northwestern University: Evanston, IL, 1993.
22. Ohtsu, M. *JCI Trans.* **1989,** *11,* 673–678.
23. Landis, E.N.; Ouyang, C.; Shah, S.P. *J. Acoustic Emission* **1992,** *10,* S97–S103.
24. Swartz, S.E.; Go, C.G. *Exper. Mech.* **1984,** *24,* 129–134.
25. Landis, E.N.; Shah, S.P. Submitted for publication.
26. Sachse, W.; Kim, K.Y. In *Review of Progress in Quantitative Nondestructive Evaluation, 6A;* Thompson, D.O.; Chimenti, D.E., Eds.; Plenum: New York, 1986; pp 311-320.
27. Jia, Z.L.; Shah, S.P. In *Proceedings from the International Conference on Nondestructive Testing of Concrete in the Infrastructure,* June 9–11, 1993; Society for Experimental Mechanics; Dearborn, MI; pp 179–191.
28. Slate, F.O.; Hover, K.C. In *Fracture Mechanics of Concrete: Material Characterization and Testing;* Carpinteri, A.; Ingraffea, A.R., Eds.; Martinus Nijhoff: Boston, 1984; pp 137–160.
29. Jenq, Y.-S.; Shah, S.P. *Eng. Fract. Mech.* **1985,** *21,* 1055–1069.
30. RILEM Committee on Fracture Mechanics of Concrete - Test Methods. *Mater. Struct.* **1990,** *23,* 457–460.
31. Lange, D.A.; Jennings, H.M.; Shah, S.P. *J. Am. Ceramic Soc.* **1993,** *76,* 589–597.
32. Zampini, D.; Jennings, H.M.; Shah, S.P. Submitted for publication.